ACS APPLIED MATERIALS & INTERFACES

www.acsami.org

Research Article

Influence of Au, Pt, and C Seed Layers on Lithium Nucleation Dynamics for Anode-Free Solid-State Batteries

André Müller,* Luis Paravicini, Jędrzej Morzy, Maximilian Krause, Joel Casella, Nicolas Osenciat, Moritz H. Futscher, and Yaroslav E. Romanyuk*

Cite This: *ACS Appl. Mater. Interfaces* 2024, 16, 695−703

Read Online

ACCESS | Metrics & More | Article Recommendations | Supporting Information

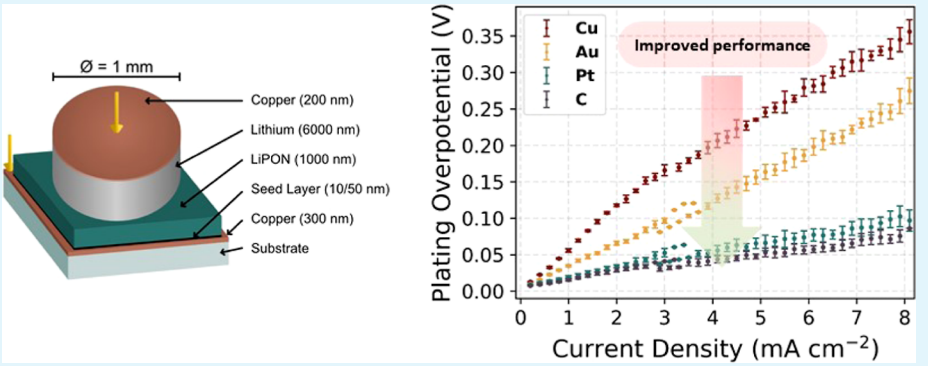

ABSTRACT: In the concept of anode-free lithium-ion batteries, cells are manufactured with a bare anode current collector where the lithium metal anode is electrochemically formed from the lithium-containing cathode during the first charge cycle. While this concept has many attractive aspects from a manufacturing and energy density standpoint, stable plating and stripping remain challenging. We have investigated gold, platinum, and amorphous carbon as seed layers placed between the copper current collector and the lithium phosphorus oxynitride thin-film solid electrolyte. These layers guide lithium nucleation and improve the plating and stripping dynamics. All seed layers facilitate reversible lithium plating and stripping even at high current densities up to 8 mA cm^{-2}. Of particular note is the amorphous carbon seed layer, which allowed a significant reduction in plating potential from 300 mV to as low as 50 mV. These results underscore the critical role of seed layers in improving the efficiency of anode-free solid-state batteries and open the door to simplified manufacturing of anode-free battery designs.

KEYWORDS: *seed layers, lithium plating/stripping, anode-free, solid-state battery*

1. INTRODUCTION

Solid-state batteries are considered the next generation of battery technology, offering advantages in safety and energy density.[1−5] The introduction of a solid, ionically conductive lithium-ion electrolyte in place of the organic liquid electrolyte traditionally used in lithium-ion batteries promises longer life and improved safety by eliminating flammable components. This technology also paves the way for replacing traditional graphite anodes with metallic lithium, resulting in 40−50% higher energy density.[6−10] The introduction of metallic lithium presents challenges such as high reactivity, unstable interfaces, and lithium dendrite growth due to nonuniform plating and stripping.[11] These complications can lead to current focusing, dendrite formation during battery cycling, and potentially dangerous short circuits. Furthermore, lithium metal is highly reactive, and integration into a battery is only possible under an inert atmosphere, suggesting that the use of metallic lithium films in solid-state batteries may not be practical.[12]

One potential strategy to overcome manufacturing challenges and further increase energy density is to move away from lithium foils to anode-free solid-state batteries (AFSSBs) or a "zero lithium excess" manufacturing process.[13] Here, the battery is manufactured in the discharged state with a lithium-containing cathode and a bare anode-side current collector (CC).[14−17] This concept not only increases the energy density by reducing the battery volume and weight but also reduces the handling and manufacturing complexity. The lithium metal anode is then formed electrochemically during the first charge cycle by electroplating lithium present in the cathode. Therefore, mechanisms that control the nucleation and growth

Received: October 2, 2023
Revised: November 24, 2023
Accepted: December 8, 2023
Published: December 21, 2023

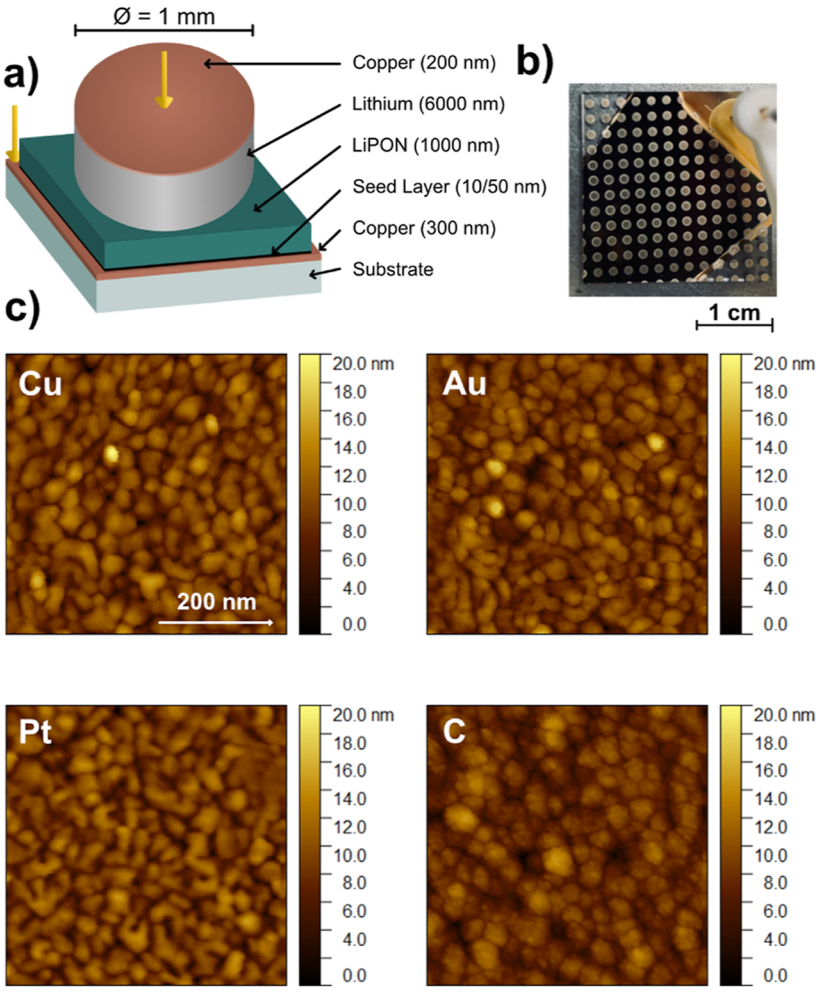

Figure 1. (a) Schematic illustration of the device configuration: Cu/Seed layer/LiPON/Li/Cu. (b) Photograph showing separate lithium reservoirs (1 mm diameter) for distinct cells. (c) AFM micrographs of bare copper CC, gold, platinum, and amorphous carbon seed layers. The scale bar is the same for all micrographs.

of lithium metal are crucial to the success of AFSSBs.[18] While the concept of anode-free batteries had been previously demonstrated in traditional liquid systems,[17,19−22] its implementation in solid-state systems lagged.

Early research on AFSSBs began with a study by Neudecker et al.[23] in 2000. This work involved the fabrication of an anode-free thin film battery with a copper current collector, a lithium phosphorus oxynitride (LiPON) electrolyte, and a lithium cobalt oxide cathode using magnetron sputtering. The battery retained 80% of its original capacity after 1000 cycles. Later research shifted the focus to an anode-free battery with a seed layer. A seed layer is a comparable thin layer deposited between the anodic current collector and the solid electrolyte. It provides nucleation sites for lithium metal growth and can improve battery performance and stability.[13] This direction was notably advanced by Lee et al.[24] at Samsung in 2020. Their research demonstrated an AFSSB with a silver−carbon nanocomposite layer and a sulfide electrolyte, achieving more than 1000 cycles and an energy density of more than 900 W h L^{-1}. The study of Feng et al.[25] demonstrated the effectiveness of carbon seed layers in improving the air stability of LLZO when deposited on a garnet-based electrolyte, thereby reducing the area-specific resistance of the Li/LLZO interface. Building on this, Futscher et al.[26] explored the use of amorphous carbon seed layers. These layers facilitated uniform lithium plating, effectively prevented dendrite formation, and increased the critical current density to 8 mA cm^{-2}.

Besides carbon interlayers and mixtures of carbon composites, noble metals such as platinum and gold seed layers have also been explored. Studies on platinum[27,28] revealed the effects of lithium plating and stripping reactions with platinum current collectors on LiPON, increasing the lithium nucleation number density compared to copper CC. Microscopic observations provided insights into the interactions between platinum and lithium. Recent studies of gold seed layers[29−34] have shown their role in improving the efficiency and lifetime of AFSSBs. The work of Krauskopf et al.[32] has investigated the effects of morphological instability of lithium metal anodes in the presence of gold seed layers. They have shown that the use of a lithium-alloying gold layer delays the penetration of lithium metal into the garnet electrolyte and penetration occurs only after the alloy phases are fully formed. This line of research was further explored by Kim et al.,[33] who demonstrated effective regulation of lithium distribution on LLZO by modifying the surface with an interlayer. They proposed that the seed interlayer serves two main functions during battery operation: it acts as a dynamic buffer for the redistribution of lithium and as a matrix layer for facile lithium precipitation.

https://doi.org/10.1021/acsami.3c14693
ACS Appl. Mater. Interfaces 2024, 16, 695−703

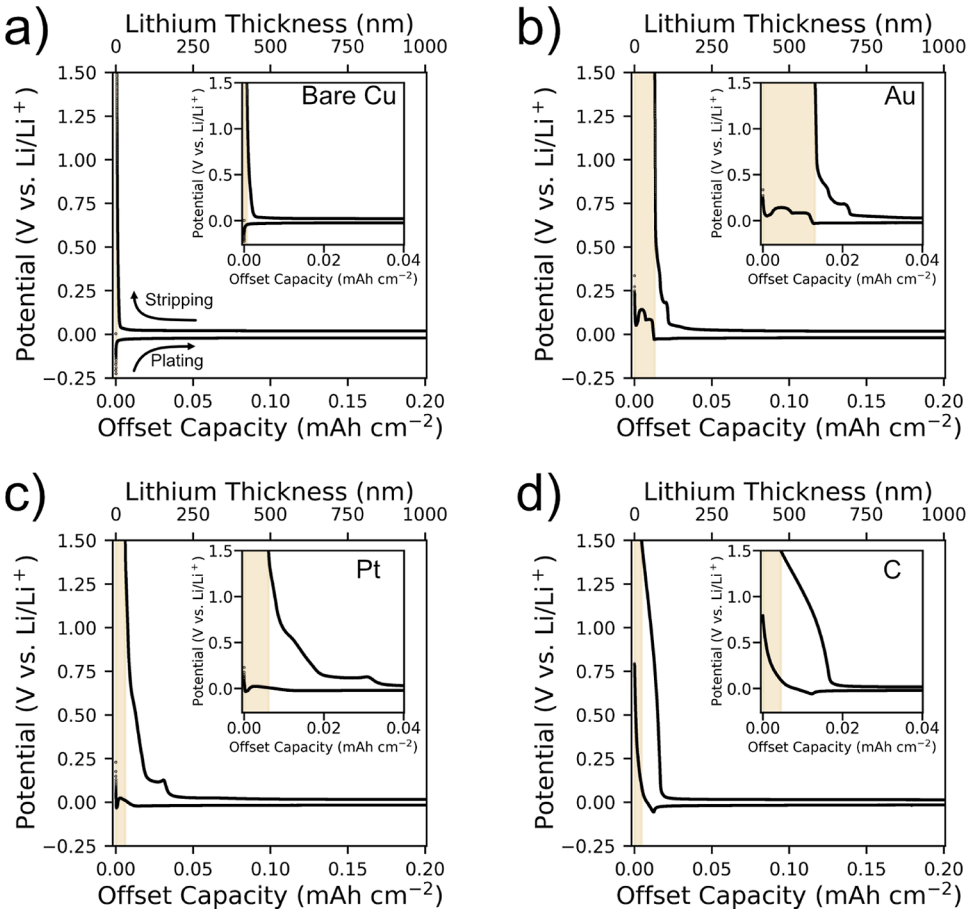

Figure 2. Effect of seed layers on lithium metal plating and stripping during the first cycle at a current density of 0.2 mA cm^{-2} and an offset capacity of 0.2 mA h cm^{-2}. Distinct voltage profiles were observed during lithium plating and stripping for a bare copper current collector (a) and different seed layer materials of gold, platinum, and amorphous carbon (b–d). Au and Pt show alloying behavior, and C shows lithium intercalation behavior. Areas highlighted in yellow indicate lithium loss in the first cycle. The inset shows zoomed data highlighting different lithiation behaviors.

This work aims to compare the impact of different seed layers — gold, platinum, and amorphous carbon — on lithium plating and stripping in a thin-film configuration. The seed layers are placed between the bare copper CC—since the early day being used as conventional current collectors on the anode side[35]—and the LiPON solid electrolyte. The resulting configurations were tested in half-cell structures, and the evolution of the overpotential and the relationship between lithium plating/stripping, nucleation kinetics, and alloying properties of each seed layer were analyzed. By comparing different seed layers, amorphous carbon was found to be a cost-effective alternative to precious metals, reducing the rise in overpotential by up to 70%.

2. RESULTS AND DISCUSSION

We fabricated thin-film stacks to study different seed layer materials in the following architecture: Cu/seed layer/LiPON/Li/Cu, as shown in Figure 1a, and compared with the reference architecture: Cu/LiPON/Li/Cu. The use of shadow masks allowed us to evaporate individual areas (1 mm diameter dots) of the lithium reservoir as separate cells (Figure 1b). The LiPON solid electrolyte was chosen due to its successful track record in facilitating reversible cycling of lithium in AFSSBs, especially when combined with copper as a current collector.[23] The amorphous nature of LiPON isolates the surface morphology and chemistry from other potential obstacles, such as the presence of grain boundaries—a notable advantage over crystalline electrolytes such as LLZO.[36] In addition, LiPON's ability to form a thin yet stable passivation layer with the lithium metal helps reduce lithium loss during subsequent cycling.[37,38]

Gold, platinum, and amorphous carbon were chosen as the seed layer materials. A 10 nm thick layer of gold was deposited by thermal evaporation. Platinum and carbon layers were deposited by RF magnetron sputtering to achieve thicknesses of 10 nm for platinum and 50 nm for carbon. Initial tests showed that the 10 nm gold layer in our thin film battery showed superior cycling performance compared to thicker layers (100 nm gold layer, Figures S1 and S2). The comparatively poor performance of thicker films compared with thinner films is due to the longer lithium diffusion length. This results in greater internal stress during lithium insertion/extraction.[39] Amorphous carbon, on the other hand, was previously shown to perform best at a thickness of 50 nm.[26]

The atomic force microscopy (AFM) images shown in Figure 1c reveal surface morphologies that are comparable for all seed layers. All materials exhibit a smooth texture with an RMS roughness of 2.2 nm ± 0.1 nm. There are no significant morphological differences between the different seed layers. For a complete overview, see Table S1 in the ESI. Therefore, it is unlikely that the morphological characteristics of the seed layers have an influence on the lithium plating and stripping

https://doi.org/10.1021/acsami.3c14693
ACS Appl. Mater. Interfaces 2024, 16, 695−703

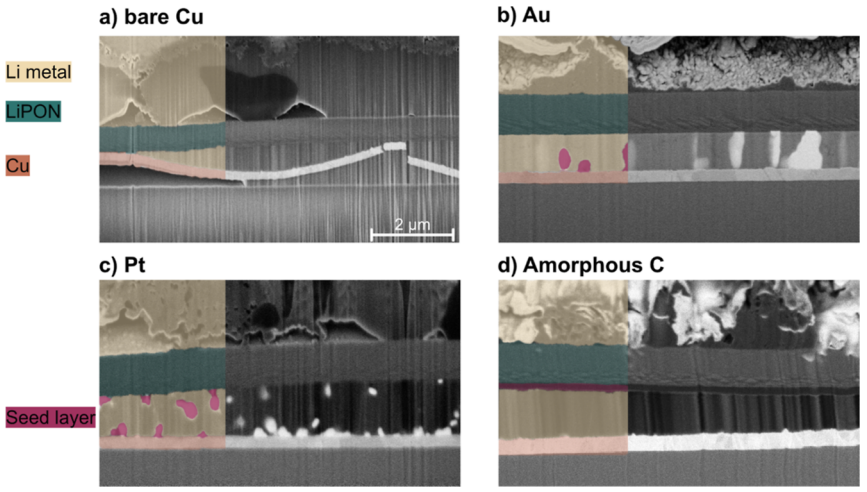

Figure 3. Cross-sectional SEM micrographs of the current collector-solid electrolyte interface with 0.2 mA h cm^{-2} (1 μm) plated lithium for (a) bare copper current collector and with (b–d) gold, platinum, and amorphous carbon seed layers after the first cycle. The scale bar is the same for all micrographs. All micrographs were taken in backscattered electron mode.

processes. As a result, observed disparities can be attributed to differences in electrochemical processes and physicochemical properties such as interfacial energies, alloying energies, and so forth.

Experiments involving the plating and stripping of a dense lithium metal layer were conducted. In our study, the terms "plating and stripping" in the context of thin film anode-free half cells refer to the process of galvanostatic charging and discharging. This involves the application of a constant current, which is essential to manage the plating and stripping of lithium. We set constant current conditions for a certain duration to obtain a lithium layer of 250 nm or 1 μm depending on the experiment. In addition, we set potential limits to 1.5 V vs Li/Li^+ to avoid excessive degradation of the LiPON solid-electrolyte layer.

Figure 2a presents the representative voltage profiles for a bare copper CC and different seed materials (Figure 2b–d). Lithium metal of 0.2 mA h cm^{-2} was plated, corresponding to a thickness of 1 μm of dense lithium, using a current density of 0.2 mA cm^{-2}. Upon application of current to the bare copper CC, the voltage exhibited a sharp decrease below 0 V vs Li/Li^+, reaching a nucleation potential at −225 mV. This pattern, characterized by a rapid voltage drop followed by a flat voltage plateau at −20 mV, aligns with predictions from the nucleation and growth theory.[21]

Unlike copper, gold and platinum have unique interaction mechanisms with lithium. The gold layer interacts with lithium to form Li_x-Au alloy phases and has a specific solubility range in lithium metal.[22] Thus, lithium alloys with gold form a saturated phase prior to the formation of pure lithium metal. Similarly, the platinum layer, with its distinct solubility properties, provides a range of potential nucleation sites.[40] The lithium metal plating process on gold and platinum nucleation layers is characterized by two separate potential plateaus, followed by a potential drop that signals the start of lithium plating. The plating potential for these processes reaches its minimum at approximately −30 mV. This reduced nucleation potential is attributed to the identical crystal structures of pure lithium metal (β-Li) and the solid solution surface layer, which effectively reduce nucleation barriers.[22]

Lithium plating in the presence of amorphous carbon seed layers shows a markedly different voltage profile; it shows a slower decrease in potential. This voltage decline corresponds to the initial lithiation of the carbon seed layer, indicating an intercalation behavior similar to graphite. In fact, amorphous carbon seed layers can host up to 200 mA h g^{-1} between 5 mV and 1 V vs Li/Li^+.[41] The drop is followed by a potential minimum at −55 mV before cells with a carbon seed layer also reach a constant voltage plateau. Despite these differences, a consistent observation at low current densities across the materials is the emergence of a flat voltage plateau at about −20 mV.

Irreversible capacity loss in the first cycle also varies between seed materials and is highlighted by the yellow areas (Figure 2). While almost no loss is observed for the bare copper CC reference, alloying materials such as gold and platinum show the greatest losses. Gold has the highest lithium loss with a peak value of 13 μA h cm^{-2}, corresponding to 65 nm of dense lithium metal, while platinum has a loss of about 6 μA h cm^{-2}. The greater lithium loss observed in gold during the first cycle could be attributed to the different reactivities of gold and platinum with lithium. Carbon shows the lowest irreversible lithium loss of the seed layers of about 4.5 μA h cm^{-2} in the first cycle.

To better understand the plated lithium morphology, the influence of various seed layers, and irreversible lithium loss, we conducted FIB-scanning electron microscopy (SEM) analysis under cryogenic conditions. Figure 3 shows cross-sectional micrographs of the reference cell with bare copper CC and cells with gold, platinum, and amorphous carbon seed layers. Each cell has 0.2 mA h cm^{-2} of lithium metal electrochemically plated during the first cycle, which equals 1 μm of dense lithium metal.

In the copper reference cell (see Figure 3a), two large cracks are observed in the CC. These cracks can be attributed to the nonuniform deposition of lithium, which exerts mechanical forces on the copper CC, ultimately leading to its failure. This failure mechanism is a common problem in thin-film batteries, as investigated in the study of Motoyama et al.[42] The formation of cracks in the copper CC creates energetically favorable sites for lithium nucleation. This phenomenon may also explain the observed penetration and deposition of lithium beneath the copper CC, leading to the development of gaps between the substrate and the CC. Similar cracks were

https://doi.org/10.1021/acsami.3c14693
ACS Appl. Mater. Interfaces 2024, 16, 695−703

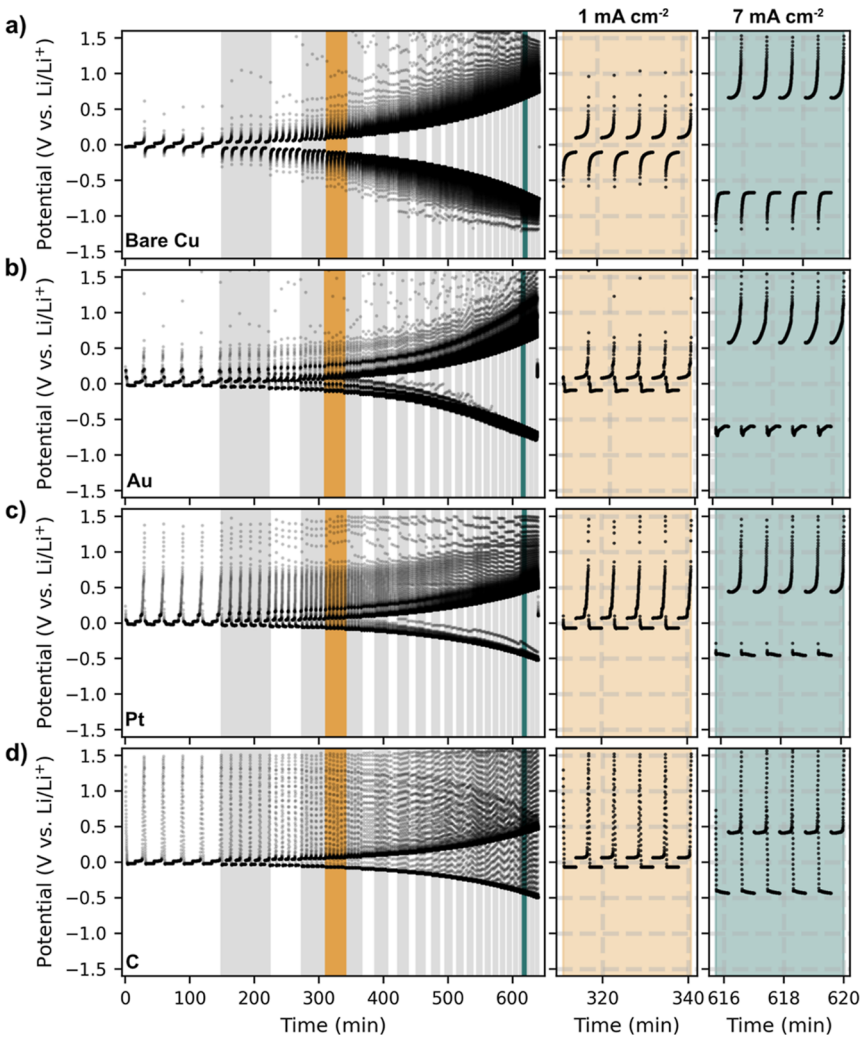

Figure 4. Effects of current density on lithium plating and stripping in thin-film cells for (a) bare copper CC, (b) gold, (c) platinum, and (d) amorphous carbon seed layer cells. The full data set in the first column cycled at current densities from 0.2 to 8 mA cm^{-2}. The regions differentiated by varying current densities are highlighted with gray shading. Each step represents an increase of 0.2 mA cm^{-2}. The second and third columns show the potential behavior at 1 mA cm^{-2} (yellow) and 7 mA cm^{-2} (green), respectively. Each density was repeated five times at an offset capacity of 0.05 mA h cm^{-2}, corresponding to 250 nm of densely plated lithium.

detected on several other cells with bare copper CC, from both the same substrate and different batches. Additional cross-sectional SEM images of these cracks and various cells are provided in the ESI.

Figure 3b–d show cross-sectional micrographs for cells with a seed layer. The introduction of seeding layers appears to facilitate more uniform lithium deposition, which in turn reduces the mechanical stress on the CC as no cracks are observed. The gold seed layer cell contains brighter particles with sizes on the order of 1 μm within the plated lithium layer, which are likely Li–Au alloy clusters. Interestingly, the 10 nm thin gold seed layer agglomerates and forms such clusters instead of remaining in the form of a uniformly thin alloy layer. Inaoka et al.[43] reported similar behavior at the Li/Li_3PS_4 interface, where the gold agglomerates into clusters. The platinum seed layer, which also forms an alloy with lithium, shows a more uniform distribution of similar but smaller clusters in the lithium metal layer. In contrast, the amorphous carbon seed layer maintains its integrity. The lithium passes through the carbon layer similarly as in our previous work[26] and facilitates the formation of a dense and uniform lithium metal layer between the current collector and carbon interlayer.

We observed high irreversible lithium losses in the first cycle for alloying materials, especially gold and platinum, which may be related to cluster structures. Initially, gold and platinum seed layers spread uniformly over the bare copper CC (Figure 1). However, during plating, these seed layers agglomerate and form alloy clusters within the lithium layer. We speculate that only surface lithium is removed, with the remainder "trapped" inside, possibly explaining the reduced lithium loss in platinum due to its smaller area/volume ratio. In addition, carbon cells show higher irreversible capacity loss than our reference copper CC, possibly related to the formation of a Li-containing interphase (lighter contrast) seen in FIB-SEM micrographs at the lithium–carbon interface.[44]

To investigate the effect of varying current densities for lithium plating and stripping, cells were cycled at current densities ranging from 0.2 to 8 mA cm^{-2} in increments of 0.2 mA cm^{-2}, as shown in Figure 4. Each current density increment was repeated five times and maintained for a time

https://doi.org/10.1021/acsami.3c14693
ACS Appl. Mater. Interfaces 2024, 16, 695–703

corresponding to an offset capacity of 0.05 mA h cm^{-2}, equivalent to plating 250 nm of dense lithium metal.

Figure 4a shows the behavior of the reference sample with a bare CC. As the current density increases, there is a corresponding increase in potential. It is noteworthy that the half-cells do not exhibit a critical current density even at an upper limit of 8 mA cm^{-2}. The critical current density is the maximum current that a cell can sustain before it shorts out. This behavior indicates inherent stability even at high current densities[45−47] and demonstrates the robustness of the thin-film system. The voltage profiles at 1 and 7 mA cm^{-2} are shown in the second and third columns of Figure 4. In the copper reference cell at 7 mA cm^{-2}, a stable plating plateau is observed at −750 mV. This plateau is consistent with the growth region identified in previous research by Pei et al.,[21] and this stability is maintained at high current densities. In particular, the 250 nm lithium plating remains consistent, avoiding the exponential potential drops typically associated with void formation.

Figure 4b−d show the voltage profiles for cells with gold, platinum, and amorphous carbon seed layers. These cells, like the bare copper CC cells, do not reach a short circuit at the applied current density of 8 mA cm^{-2} during the plating of 250 nm dense lithium. For all seed materials tested, the lithiation plateaus are consistently observed during both the plating and stripping processes, even at higher current densities of 1 and 7 mA cm^{-2}. A comparison of the bare copper CC with other seed layers reveals differences in their plating and stripping dynamics. The introduction of a thin gold seed layer improves stability, with its plateau stabilizing at −680 mV. This represents a reduction in overpotential of up to 10% at the highest current density tested, 8 mA cm^{-2}. In contrast, the platinum and carbon seed layers establish their voltage plateaus at −520 and −490 mV, respectively.

Figure 5 provides a comparison of the evolution of the plating overpotential as a function of the current density for all

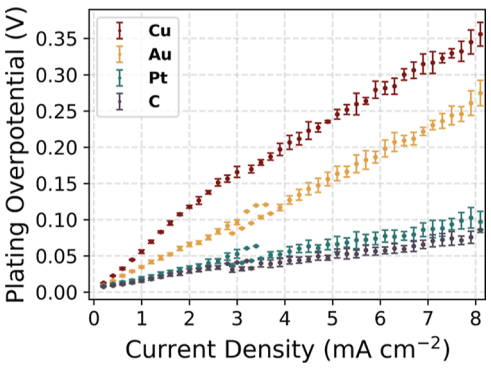

Figure 5. Plating overpotential response to the current density for seed layers. The potentials presented here have been adjusted to account for polarization effects due to electrolyte resistance. The error bars show the standard deviation of the data from three individual cells.

of the seeds. The standard deviation between individual cells per seed layer does not exceed 10%. To account for polarization effects due to electrolyte resistance, the potentials shown here have been adjusted accordingly. More detailed information on the methodology used to evaluate the plating overpotential in the growth region,[21] including data processing and statistical analysis, can be found in the ESI Section 3.

A consistent linear trend of the increase in the plating overpotential with increasing current density is observed for all seeds. The bare copper CC cell shows the steepest increase, reaching a peak overpotential of 325 mV at a current density of 8 mA cm^{-2}. The gold seed layer cell has a slightly lower rise in overpotential, reaching a maximum of 250 mV, while platinum and carbon have the lowest overpotentials of less than 100 mV at the highest current density measured.

The performance of carbon as a seed layer is characterized by a minimal increase in the plating overpotential at higher current densities, reflecting stable electrochemical plating and hence less overpotential evolution. This stability is due to the intact amorphous carbon seed layer between the current collector and the solid electrolyte—as shown in Figure 3—which ensures homogeneous plating, optimal current distribution, and minimized overpotential. It ensures uniform Li-ion diffusion, enhances surface reaction rates, inhibits lithium filament growth, and improves the reversibility of lithium plating. Our results show that carbon and lithium−platinum alloys provide better performance in lithium plating/stripping and overall battery efficiency through overpotential reduction compared with lithium−gold alloys. In addition, the promising results of two-component interlayers, namely silver/carbon[24] and gold/carbon,[22] confirm these findings.

3. CONCLUSIONS

We investigated anode-free half cells with seed layers comprising gold, platinum, or amorphous carbon placed between the LiPON solid-state electrolyte and the bare copper CC. The formation of a dense lithium metal layer between the copper CC and LiPON, which could be repeatedly plated and stripped, was demonstrated. All cells withstood current densities up to 8 mA cm^{-2} without short-circuiting, demonstrating the reliability of the thin-film configuration. Gold and platinum seed layers alloyed with lithium early in the plating process, facilitating uniform lithium metal plating on the current collector. As these layers agglomerate, they form alloy clusters distributed within the deposited lithium layer, preventing the mechanical failure of the current collector. The amorphous carbon seed layer maintains its integrity and is characterized by a uniform, dense lithium metal layer between the current collector and the seed layer. Platinum and amorphous carbon cells exhibit the lowest overpotential evolution. Amorphous carbon has been found to be a viable and cost-effective alternative to noble metals as a seed layer material.

4. EXPERIMENTAL DETAILS

4.1. Fabrication. Prior to deposition, soda-lime glass substrates were thoroughly cleaned with 2-propanol. After the substrates were cleaned, a layer of copper (Cu 99.999%, Thermo Fisher Scientific) with a thickness of 250 nm was thermally evaporated onto the substrates using a Nexdep evaporator (Angstrom Engineering Inc.) at a rate of 1 Å s^{-1}.

The sequence continued with the deposition of the seed layers. A 10 nm thick layer of gold (Au 99.99%, Heimerle + Meule GmbH Scheideanstalt) was thermally evaporated onto the copper current collector using the Angstrom Engineering Inc. system at a rate of 0.2 Å s^{-1}. Platinum (Pt 99.99%, Plasmaterials) and amorphous carbon (99.9% pure graphite, Mo-bonded, Plansee SE) were deposited by RF magnetron sputtering using an Orion sputtering system (AJA International Inc.) at thicknesses of 10 and 50 nm, respectively. The rate for platinum was 2.5 nm min^{-1} and for carbon 0.8 nm min^{-1}.

https://doi.org/10.1021/acsami.3c14693
ACS Appl. Mater. Interfaces 2024, 16, 695−703

Lithium−phosphorus oxynitride (LiPON) solid-electrolyte was then RF magnetron sputtered onto the current collector/seed layer stack. This deposition was performed unheated and resulted in a 1 μm thick LiPON layer using the cosputtering technique with 2″ targets of Li_3PO_4 (99.95%, Kurt J Lesker Co., rate approximately 0.7 nm min^{-1}) and Li_2O (99.9%, Toshima Manufacturing, rate approximately 0.6 nm min^{-1}) in a N_2 atmosphere (flow set to 50 SCCM) at powers of 100 and 120 W, respectively, and a working pressure of 4×10^{-3} mbar. The target-to-substrate distance was set to 25 cm.

After the solid electrolyte was deposited, a layer of lithium (99+%, Thermo Fisher Scientific) was added by thermal evaporation at a rate of 25 Å s^{-1}, forming a 6 μm thick layer (Nexdep evaporator) with 0.1 cm diameter shadow masks to evaporate individual lithium reservoirs as separate cells.

A 100 nm layer of copper was thermally deposited on top of lithium as the final step of the protocol. Throughout the deposition processes, a quartz microbalance was used to ensure the precise control of the film thicknesses.

4.2. Characterization. Atomic force microscopy took place in air by employing the ScanAnlyst tapping mode (Bruker Icon 3). A 2.5 μm × 2.5 μm area was scanned at a resolution of 256 × 256 pixels. Data analysis was performed with GWyddion 2.62.

Further analysis was performed using cross-sectional scanning electron microscopy. A Helios 600i TFS FIB/SEM system with a cryogenic stage was operated at −140 °C. A protective carbon layer was deposited prior to the FIB milling. The micrographs shown were taken in backscattered electron mode (2 kV and 0.69 nA).

The electrochemical characterization process was performed under an Ar atmosphere at room temperature with a Squidstat potentiostat (Admiral Instruments). A detailed protocol can be seen in Supporting Information Section 5.

■ ASSOCIATED CONTENT

Supporting Information

The Supporting Information is available free of charge at https://pubs.acs.org/doi/10.1021/acsami.3c14693.

Table summarizing AFM parameters; influence of 100 nm Au seed layer on Li plating/stripping; description of overpotential calculation methodology; cross-sectional SEM images of cracks in bare copper layers; interphase formation at the carbon seed layer; and detailed cycling procedure used for plating and stripping (PDF)

■ AUTHOR INFORMATION

Corresponding Authors

André Müller − *Laboratory for Thin Films and Photovoltaics, Empa—Swiss Federal Laboratories for Materials Science and Technology, Dübendorf CH-8600, Switzerland;* orcid.org/0000-0003-2275-8034; Phone: +41 58 765 4608; Email: andre.mueller@empa.ch

Yaroslav E. Romanyuk − *Laboratory for Thin Films and Photovoltaics, Empa—Swiss Federal Laboratories for Materials Science and Technology, Dübendorf CH-8600, Switzerland*; Email: yaroslav.romanyuk@empa.ch

Authors

Luis Paravicini − *Laboratory for Thin Films and Photovoltaics, Empa—Swiss Federal Laboratories for Materials Science and Technology, Dübendorf CH-8600, Switzerland*

Jędrzej Morzy − *Laboratory for Thin Films and Photovoltaics, Empa—Swiss Federal Laboratories for Materials Science and Technology, Dübendorf CH-8600, Switzerland;* orcid.org/0000-0003-0770-461X

Maximilian Krause − *Laboratory for Thin Films and Photovoltaics, Empa—Swiss Federal Laboratories for Materials Science and Technology, Dübendorf CH-8600, Switzerland*

Joel Casella − *Laboratory for Thin Films and Photovoltaics, Empa—Swiss Federal Laboratories for Materials Science and Technology, Dübendorf CH-8600, Switzerland;* orcid.org/0000-0002-2098-2983

Nicolas Osenciat − *Laboratory for Thin Films and Photovoltaics, Empa—Swiss Federal Laboratories for Materials Science and Technology, Dübendorf CH-8600, Switzerland*

Moritz H. Futscher − *Laboratory for Thin Films and Photovoltaics, Empa—Swiss Federal Laboratories for Materials Science and Technology, Dübendorf CH-8600, Switzerland;* orcid.org/0000-0001-8451-5009

Complete contact information is available at: https://pubs.acs.org/10.1021/acsami.3c14693

Author Contributions

A.M.: conceptualization, methodology, formal analysis, investigation, data curation, writing—original draft, visualization; L.P., J.M., M.K., J.C., N.O.: investigation; M.H.F.: conceptualization, formal analysis; Y.E.R.: conceptualization, supervision, project administration, funding acquisition. All authors contributed to the manuscript writing and revision.

Notes

The authors declare no competing financial interest.

■ ACKNOWLEDGMENTS

This work was supported by the Strategic Focus Area—Advanced Manufacturing of the ETH Domain (project "SOL4BAT"). M.H.F. is supported by a Rubicon Fellowship from The Netherlands Organization for Scientific Research (NWO). The project is supported by the European Union's Horizon 2020 research and innovation programme (grant no. 95817) and the Swiss Federal Office of Energy (SFOE, grant no. SI/502460-01). Support from the Laboratory of Ion Beam Physics and the Scientific Center for Optical and Electron Microscopy (ScopeM) of the Swiss Federal Institute of Technology (ETHZ) for the cryo-FIB-SEM measurements is gratefully acknowledged.

■ REFERENCES

(1) Wang, C.-Y.; Liu, T.; Yang, X.-G.; Ge, S.; Stanley, N. V.; Rountree, E. S.; Leng, Y.; McCarthy, B. D. Fast charging of energy-dense lithium-ion batteries. *Nature* **2022**, *611*, 485−490.

(2) Balaish, M.; Gonzalez-Rosillo, J. C.; Kim, K. J.; Zhu, Y.; Hood, Z. D.; Rupp, J. L. M. Processing thin but robust electrolytes for solid-state batteries. *Nat. Energy* **2021**, *6*, 227−239.

(3) Li, C.; Wang, Z.-y.; He, Z.-j.; Li, Y.-j.; Mao, J.; Dai, K.-h.; Yan, C.; Zheng, J.-c. An advance review of solid-state battery: Challenges, progress and prospects. *Sustainable Mater. Technol.* **2021**, *29*, No. e00297.

(4) Manthiram, A.; Yu, X.; Wang, S. Lithium battery chemistries enabled by solid-state electrolytes. *Nat. Rev. Mater.* **2017**, *2*, 16103.

(5) Janek, J.; Zeier, W. G. Challenges in speeding up solid-state battery development. *Nat. Energy* **2023**, *8*, 230−240.

(6) Janek, J.; Zeier, W. G. A solid future for battery development. *Nat. Energy* **2016**, *1*, 16141.

(7) Tarascon, J.-M.; Armand, M. Issues and challenges facing rechargeable lithium batteries. *Nature* **2001**, *414*, 359−367.

(8) Albertus, P.; Babinec, S.; Litzelman, S.; Newman, A. Status and challenges in enabling the lithium metal electrode for high-energy and low-cost rechargeable batteries. *Nat. Energy* **2017**, *3*, 16−21.

(9) Zhang, Z.; Shao, Y.; Lotsch, B.; Hu, Y.-S.; Li, H.; Janek, J.; Nazar, L. F.; Nan, C.-W.; Maier, J.; Armand, M.; Chen, L. New horizons for inorganic solid state ion conductors. *Energy Environ. Sci.* **2018**, *11*, 1945−1976.
(10) Goodenough, J. B.; Kim, Y. Challenges for Rechargeable Li Batteries. *Chem. Mater.* **2010**, *22*, 587−603.
(11) Wang, J.; Ge, B.; Li, H.; Yang, M.; Wang, J.; Liu, D.; Fernandez, C.; Chen, X.; Peng, Q. Challenges and progresses of lithium-metal batteries. *Chem. Eng. J.* **2021**, *420*, 129739.
(12) Becking, J.; Gröbmeyer, A.; Kolek, M.; Rodehorst, U.; Schulze, S.; Winter, M.; Bieker, P.; Stan, M. C. Lithium-Metal Foil Surface Modification: An Effective Method to Improve the Cycling Performance of Lithium-Metal Batteries. *Adv. Mater. Interfaces* **2017**, *4*, 1700166.
(13) Zor, C.; Turrell, S. J.; Uyanik, M. S.; Afyon, S. Lithium Plating and Stripping: Toward Anode-Free Solid-State Batteries. *Advanced Energy and Sustainability Research*; Wiley, 2023; p 2300001.
(14) Weber, R.; Genovese, M.; Louli, A. J.; Hames, S.; Martin, C.; Hill, I. G.; Dahn, J. R. Long cycle life and dendrite-free lithium morphology in anode-free lithium pouch cells enabled by a dual-salt liquid electrolyte. *Nat. Energy* **2019**, *4*, 683−689.
(15) Assegie, A. A.; Cheng, J.-H.; Kuo, L.-M.; Su, W.-N.; Hwang, B.-J. Polyethylene oxide film coating enhances lithium cycling efficiency of an anode-free lithium-metal battery. *Nanoscale* **2018**, *10*, 6125−6138.
(16) Cohn, A. P.; Muralidharan, N.; Carter, R.; Share, K.; Pint, C. L. Anode-Free Sodium Battery through in Situ Plating of Sodium Metal. *Nano Lett.* **2017**, *17*, 1296−1301.
(17) Qian, J.; Adams, B. D.; Zheng, J.; Xu, W.; Henderson, W. A.; Wang, J.; Bowden, M. E.; Xu, S.; Hu, J.; Zhang, J. Anode-Free Rechargeable Lithium Metal Batteries. *Adv. Funct. Mater.* **2016**, *26*, 7094−7102.
(18) Heubner, C.; Maletti, S.; Auer, H.; Hüttl, J.; Voigt, K.; Lohrberg, O.; Nikolowski, K.; Partsch, M.; Michaelis, A. From Lithium-Metal toward Anode-Free Solid-State Batteries: Current Developments, Issues, and Challenges. *Adv. Funct. Mater.* **2021**, *31*, 2106608.
(19) Kwon, H.; Lee, J.-H.; Roh, Y.; Baek, J.; Shin, D. J.; Yoon, J. K.; Ha, H. J.; Kim, J. Y.; Kim, H.-T. An electron-deficient carbon current collector for anode-free Li-metal batteries. *Nat. Commun.* **2021**, *12*, 5537.
(20) Zhang, S. S.; Fan, X.; Wang, C. A tin-plated copper substrate for efficient cycling of lithium metal in an anode-free rechargeable lithium battery. *Electrochim. Acta* **2017**, *258*, 1201−1207.
(21) Pei, A.; Zheng, G.; Shi, F.; Li, Y.; Cui, Y. Nanoscale Nucleation and Growth of Electrodeposited Lithium Metal. *Nano Lett.* **2017**, *17*, 1132−1139.
(22) Yan, K.; Lu, Z.; Lee, H.-W.; Xiong, F.; Hsu, P.-C.; Li, Y.; Zhao, J.; Chu, S.; Cui, Y. Selective deposition and stable encapsulation of lithium through heterogeneous seeded growth. *Nat. Energy* **2016**, *1*, 16010.
(23) Neudecker, B. J.; Dudney, N. J.; Bates, J. B. Lithium-Free" Thin-Film Battery with In Situ Plated Li Anode. *J. Electrochem. Soc.* **2000**, *147*, 517−523.
(24) Lee, Y.-G.; Fujiki, S.; Jung, C.; Suzuki, N.; Yashiro, N.; Omoda, R.; Ko, D. S.; Shiratsuchi, T.; Sugimoto, T.; Ryu, S.; et al. High-energy long-cycling all-solid-state lithium metal batteries enabled by silver−carbon composite anodes. *Nat. Energy* **2020**, *5*, 299−308.
(25) Feng, W.; Dong, X.; Zhang, X.; Lai, Z.; Li, P.; Wang, C.; Wang, Y.; Xia, Y. Li/Garnet Interface Stabilization by Thermal-Decomposition Vapor Deposition of an Amorphous Carbon Layer. *Angew. Chem., Int. Ed.* **2020**, *59*, 5346−5349.
(26) Futscher, M. H.; Amelal, T.; Sastre, J.; Müller, A.; Patidar, J.; Aribia, A.; Thorwarth, K.; Siol, S.; Romanyuk, Y. E. Influence of amorphous carbon interlayers on nucleation and early growth of lithium metal at the current collector-solid electrolyte interface. *J. Mater. Chem. A* **2022**, *10*, 15535−15542.
(27) Yamamoto, T.; Sugiura, Y.; Iwasaki, H.; Motoyama, M.; Iriyama, Y. Freestanding all-solid-state rechargeable lithium batteries with in-situ formed positive electrodes. *Solid State Ionics* **2019**, *337*, 19−23.
(28) Motoyama, M.; Ejiri, M.; Yamamoto, T.; Iriyama, Y. In Situ Scanning Electron Microscope Observations of Li Plating/Stripping Reactions with Pt Current Collectors on LiPON Electrolyte. *J. Electrochem. Soc.* **2018**, *165*, A1338−A1347.
(29) Chen, W.; Fu, M.; Zhao, Q.; Zhou, A.; Huang, W.; Wang, J. Au-modified 3D carbon cloth as a dendrite-free framework for Li metal with excellent electrochemical stability. *J. Alloys Compd.* **2021**, *871*, 159491.
(30) Huang, M.; Yao, Z.; Yang, Q.; Li, C. Consecutive Nucleation and Confinement Modulation towards Li Plating in Seeded Capsules for Durable Li-Metal Batteries. *Angew. Chem., Int. Ed.* **2021**, *60*, 14040−14050.
(31) Xu, T.; Hou, L.; Yan, C.; Hou, J.; Tian, B.; Yuan, H.; Kong, D.; Wang, H.; Li, X.; Wang, Y.; Zhang, G. Uniform lithium deposition guided by Au nanoparticles in vertical-graphene/carbon-cloth skeleton for dendrite-free and stable lithium metal anode. *Scr. Mater.* **2023**, *229*, 115352.
(32) Krauskopf, T.; Dippel, R.; Hartmann, H.; Peppler, K.; Mogwitz, B.; Richter, F. H.; Zeier, W. G.; Janek, J. Lithium-Metal Growth Kinetics on LLZO Garnet-Type Solid Electrolytes. *Joule* **2019**, *3*, 2030−2049.
(33) Kim, S.; Jung, C.; Kim, H.; Thomas-Alyea, K. E.; Yoon, G.; Kim, B.; Badding, M. E.; Song, Z.; Chang, J.; Kim, J.; Im, D.; Kang, K. The Role of Interlayer Chemistry in Li-Metal Growth through a Garnet-Type Solid Electrolyte. *Adv. Energy Mater.* **2020**, *10*, 1903993.
(34) Haslam, C.; Sakamoto, J. Stable Lithium Plating in "Lithium Metal-Free" Solid-State Batteries Enabled by Seeded Lithium Nucleation. *J. Electrochem. Soc.* **2023**, *170*, 040524.
(35) Zhu, P.; Gastol, D.; Marshall, J.; Sommerville, R.; Goodship, V.; Kendrick, E. A review of current collectors for lithium-ion batteries. *J. Power Sources* **2021**, *485*, 229321.
(36) Dussart, T.; Rividi, N.; Fialin, M.; Toussaint, G.; Stevens, P.; Laberty-Robert, C. Critical Current Density Limitation of LLZO Solid Electrolyte: Microstructure vs Interface. *J. Electrochem. Soc.* **2021**, *168*, 120550.
(37) Sicolo, S.; Fingerle, M.; Hausbrand, R.; Albe, K. Interfacial instability of amorphous LiPON against lithium: A combined Density Functional Theory and spectroscopic study. *J. Power Sources* **2017**, *354*, 124−133.
(38) Cheng, D.; Wynn, T. A.; Wang, X.; Wang, S.; Zhang, M.; Shimizu, R.; Bai, S.; Nguyen, H.; Fang, C.; Kim, M.-c.; Li, W.; Lu, B.; Kim, S. J.; Meng, Y. S. Unveiling the Stable Nature of the Solid Electrolyte Interphase between Lithium Metal and LiPON via Cryogenic Electron Microscopy. *Joule* **2020**, *4*, 2484−2500.
(39) Zhang, W.-J. A review of the electrochemical performance of alloy anodes for lithium-ion batteries. *J. Power Sources* **2011**, *196*, 13−24.
(40) Sangster, J.; Pelton, A. The li-pt (lithium-platinum) system. *J. Phase Equilib.* **1991**, *12*, 678−681.
(41) Fathi, R.; Sanderson, R.; Lucas, L.; Dahn, J. The electrochemical reaction of lithium with high-capacity dense sputtered carbon. *Carbon* **2014**, *74*, 249−254.
(42) Motoyama, M.; Ejiri, M.; Nakajima, H.; Iriyama, Y. Mechanical Failure of Cu Current Collector Films Affecting Li Plating/Stripping Cycles at Cu/LiPON Interfaces. *J. Electrochem. Soc.* **2023**, *170*, 012503.
(43) Inaoka, T.; Asakura, T.; Otoyama, M.; Motohashi, K.; Sakuda, A.; Tatsumisago, M.; Hayashi, A. Tin Interlayer at the Li/Li3PS4 Interface for Improved Li Stripping/Plating Performance. *J. Phys. Chem. C* **2023**, *127*, 10453−10458.
(44) Bloi, L. M.; Hippauf, F.; Boenke, T.; Rauche, M.; Paasch, S.; Schutjajew, K.; Pampel, J.; Schwotzer, F.; Dörfler, S.; Althues, H.; Oschatz, M.; Brunner, E.; Kaskel, S. Mechanistic insights into the reversible lithium storage in an open porous carbon via metal cluster formation in all solid-state batteries. *Carbon* **2022**, *188*, 325−335.
(45) Sagane, F.; Ikeda, K.-i.; Okita, K.; Sano, H.; Sakaebe, H.; Iriyama, Y. Effects of current densities on the lithium plating

https://doi.org/10.1021/acsami.3c14693
ACS Appl. Mater. Interfaces 2024, 16, 695−703

morphology at a lithium phosphorus oxynitride glass electrolyte/copper thin film interface. *J. Power Sources* **2013**, *233*, 34−42.
(46) Motoyama, M.; Ejiri, M.; Iriyama, Y. In-Situ Electron Microscope Observations of Electrochemical Li Deposition/Dissolution with a LiPON Electrolyte. *Electrochemistry* **2014**, *82*, 364−368.
(47) Lu, Y.; Zhao, C.; Yuan, H.; Cheng, X.; Huang, J.; Zhang, Q. Critical Current Density in Solid-State Lithium Metal Batteries: Mechanism, Influences, and Strategies. *Adv. Funct. Mater.* **2021**, *31*, 2009925.

https://doi.org/10.1021/acsami.3c14693
ACS Appl. Mater. Interfaces 2024, 16, 695−703